

Synthesis of SnO₂ nanoparticles for formaldehyde detection with high sensitivity and good selectivity

Liping Gao^{1,a),c)}, Hao Fu^{2,3,c)}, Jiejun Zhu¹, Junhai Wang¹, Yuping Chen¹, Hongjie Liu^{2,b)}

¹School of Materials and Chemical Engineering, Chuzhou University, Chuzhou 239000, China

²Department of Science and Technology, Shiyuan College of Nanning Normal University, Nanning 530226, China

³School of Marine Sciences, Guangxi University, Nanning 530004, China

^{a)}Address all correspondence to these authors. e-mail: gaozhangping@163.com

^{b)}e-mail: hongjieliu2008@163.com

^{c)}These authors contributed equally to this work.

Received: 28 March 2020; accepted: 29 June 2020

During the detection of industrial hazardous gases, like formaldehyde (HCHO), the selectivity is still a challenging issue. Herein, an alternative HCHO chemosensor that based on the tin oxide nanoparticles is proposed, which was obtained through a facile hydrothermal method. Gas sensing performances showed that the optimal working temperature located at only 180 °C, the response value of 79 *via* 50 ppm HCHO was much higher than that of 35 at 230 °C. However, the compromised test temperature was selected as 230 °C, taking into account the faster response/recovery speeds than 180 °C, named 20/23 versus 53/60 s, respectively. The response (35) of the SnO₂ nanoparticles-based sensor to 50 ppm of HCHO is about 400% higher than that of bulk SnO₂ sensor (9), especially when the gas concentration is 1 ppm, SnO₂ nanoparticles also has a higher sensitivity which may possibly result from more exposed active sites and small size effect for nanoparticles than for bulk ones. The gas sensor based on SnO₂ nanoparticles can be utilized as a promising candidate for practical low-temperature detectors of HCHO due to its higher gas response, excellent response–recovery properties, and perfect selectivity.

Introduction

Formaldehyde is a typical toxic gas in indoor air pollution, which is often used in the manufacture of building plywood, paint, and other decorative building materials [1, 2, 3]. Besides, it is considered as a typical toxic chemical substance in environmental monitoring and assessment, which endangers the health and safety of humans and other creatures [4, 5, 6]. The most common symptoms associated with formaldehyde exposure include eye, nose, and throat irritation, which occurs when the air concentration is about 0.4–1 (ppm). High levels of formaldehyde can even cause damage to the central nervous system, blood, and immune system [7]. Therefore, it needs real-time and effective formaldehyde monitoring methods to prevent it from exceeding the dangerous threshold. Up to now, many approaches have been applied to detect HCHO, including spectrophotometry, gas chromatography, high-performance liquid chromatography, polarography, and fluorimeter [8, 9, 10, 11, 12]. However, further practical applications are limited by expensive instruments and time-consuming operation. Semiconductor gas sensors have been confirmed as a reliable

candidate for HCHO detection. Many researchers have done work on formaldehyde sensors based on different metal oxide materials, such as shuttle-like ZnO nano/microrods [13, 14], Pd nanoparticle-decorated hollow SnO₂ nanofibers, and In₂O₃ hetero-nanofibers [15, 16].

Tin dioxide (SnO₂) is a typical n-type semiconductor material with a wide band gap of 3.6 eV. Nano-sized SnO₂ has been widely used in photocatalysis, solar cells, conductive transparent glass, and harmful gas detection [17, 18, 19, 20]. Semiconductor SnO₂ has been widely used in the detection of combustible and toxic gases such as alcohol [21], acetone [22], butanone [23], and H₂S [24]. Recently, SnO₂ (SnO₂ nanowires [25], SnO₂ nanosheets [26, 27], SnO₂ nanoflowers [28, 29]) with different micro/nanostructures were synthesized and applied in the field of gas sensing. The sensing mechanism of SnO₂ mainly belongs to the surface-control gas reaction with the target gas molecules reacting with adsorbed oxygen on the surface [30]. It is determined by a lot of factors such as grain size, surface states, and oxygen adsorption quantities [31]. As the nanoparticles become smaller, the specific surface area of

the nanomaterials increases significantly, and the surface atomic ratio increases rapidly which can be in better contact with gases. Because the valences of the atoms on the surface of the nano atom are usually unsaturation, a lot of dangling bonds will be formed on the surface, that is, lots of unpaired electrons exist that are easy to bind more oxygen molecules on the surface, so that the nanoparticles possess high surface activity for the gas sensing reaction.

Currently, researchers remain committed to research how to detect HCHO with high selectivity at relatively lower working temperature. In this paper, to give the classic gas-sensing material a deeper insight between the structure and performance, fine SnO₂ nanoparticles were synthesized using a simple hydrothermal method. The as-prepared SnO₂ nanoparticles sensor showed excellent gas-sensing properties toward HCHO. The sensor exhibits the highest response (79) to 50 ppm of HCHO at 180 °C, has good selectivity for HCHO at a test temperature of 230 °C, and also has good response at low concentration, making it to be a promising candidate for practical detectors for HCHO.

Results and Discussion

The phase purity and crystal structure of the as-synthesized SnO₂ nanoparticles and nanorods were investigated by X-ray diffraction (XRD). Figure 1(b) illustrates the typical diffraction patterns of (a) bulk SnO₂ and (b) SnO₂ nanoparticles. All the peaks can be well indexed to the cassiterite SnO₂ (PDF: 41-1445, $a = b = 4.738 \text{ \AA}$, $c = 3.187 \text{ \AA}$), space group $P42/mnm$ (136) [32, 33]. No characteristic peaks were observed for other impurities, demonstrating the high purity of the as-synthesized SnO₂ nanoparticles and bulk SnO₂.

Figure 2 shows the SEM image of SnO₂ nanoparticles and bulk SnO₂. From Figs. 2(a) and 2(b), it can be seen that the products are nanoparticles mixed with tiny nanosheets (red circle). The nanoparticles and nanosheets agglomerate due to the small size. Figures 2(c) and 2(d) show the SEM images of bulk

SnO₂. From Fig. 2(c), we can see that the bulk SnO₂ are large and nonuniform in size, and some of them are broken. It can be clearly seen from Fig. 2(d) that the sample is formed by the small nano-sized particles and the particles are closely packed without void. Figure 3 shows the TEM images of SnO₂ nanoparticles. From Figs. 3(a)–3(c), it can be seen that the product is nanoparticles which mixed with a few nanosheets (red circle). The size of small nanoparticles is not more than 20 nm. The HRTEM [Fig. 3(d)] of nanoparticles displays clear lattice fringes with the spacing of 0.336 and 0.265 nm, which can be attributed to the (110) and (101) lattice planes of SnO₂. The size of the two samples is quite different, so the specific surface area of the material was calculated by the BET (Brunauer–Emmett–Teller) method. As shown in Fig. 4, the BET surface area of SnO₂ nanoparticles (42.5 m²/g) is greater than bulk SnO₂ (31.1 m²/g). Therefore, we suspect that the performance of the gas-sensing properties of SnO₂ nanoparticles would better than SnO₂ nanorods due to a larger specific surface area.

The optical properties of a semiconductor are related to both intrinsic and extrinsic effects. The photoluminescence (PL) spectrum is a suitable technique to determine the crystalline quality and the presence of impurities in the materials as well as exciton fine structures [34]. PL spectrum of the SnO₂ nanoparticles and bulk SnO₂ were measured using Xe laser (325 nm) as an excitation source [Fig. 5(a)]. Both samples display blue-green light emission peak from 430 to 490 nm and yellow-blue light emission peak near 560 nm. The blue-green light luminescence from the as-synthesized SnO₂ nanoparticles and bulk SnO₂ can be attributed to oxygen-related defects that have been introduced during growth. To further prove the existence of oxygen vacancy, X-ray photoelectron spectroscopy (XPS) characterization has provided; Fig. 5(b) shows the survey date of SnO₂ nanoparticles and bulk SnO₂. And in Fig. 5(c), O 1s core-level XPS spectrum of SnO₂ nanoparticles and bulk SnO₂: one peak at 530.21 eV is deemed as the lattice oxygen (O_L) from Sn–O–Sn, while the other one located at 531.15 eV should be attributed to oxygen vacancy

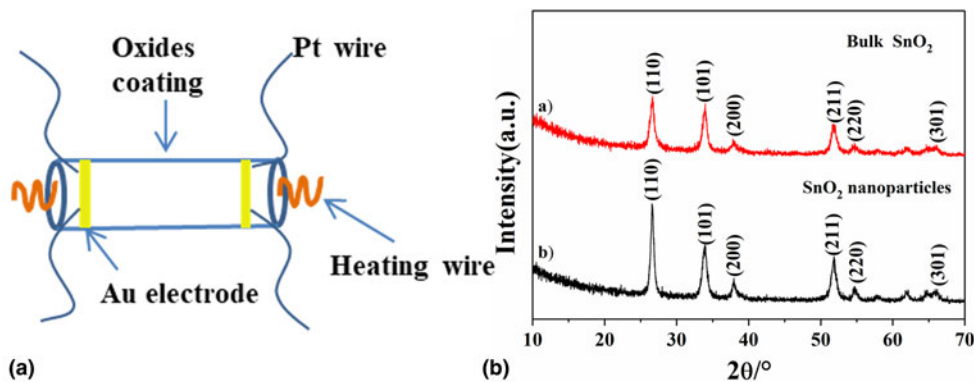


Figure 1: (a) Schematic diagram of the sensor structure and (b) XRD of (a) bulk SnO₂ and (b) SnO₂ nanoparticles.

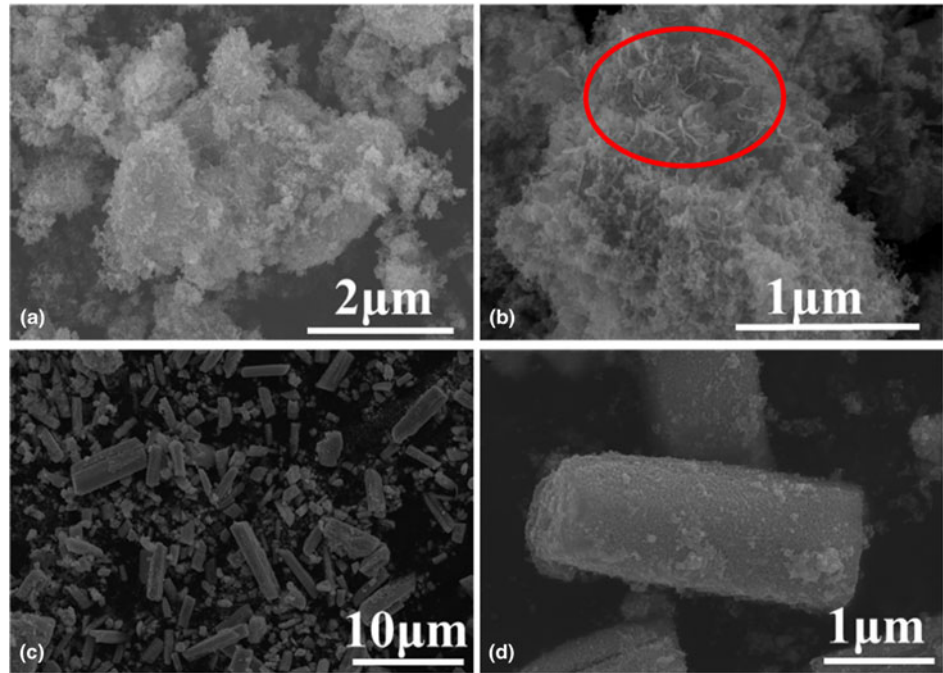


Figure 2: SEM images of (a and b) SnO₂ nanoparticles and (c and d) bulk SnO₂.

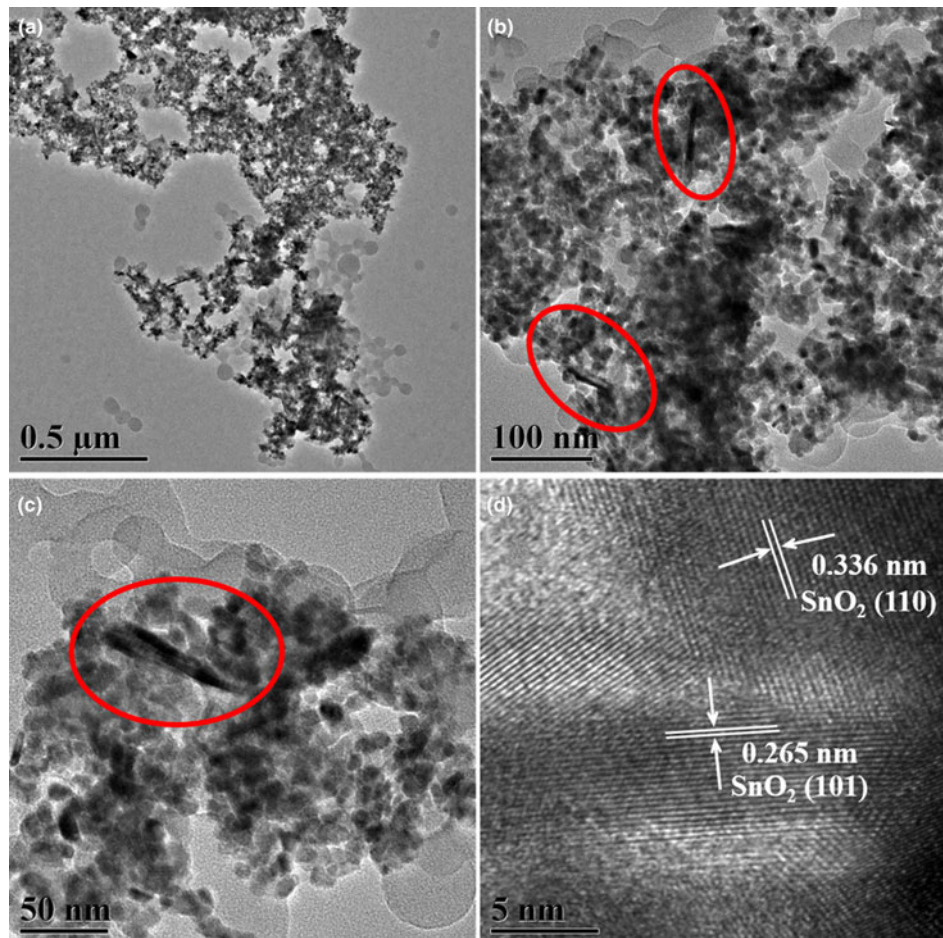


Figure 3: (a–c) TEM and (d) HRTEM images of SnO₂ nanoparticles.

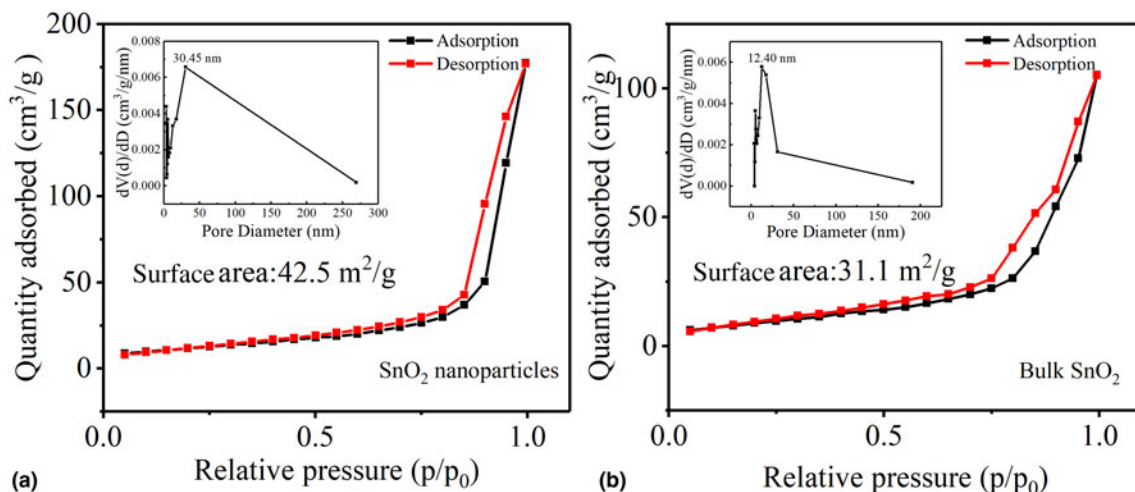


Figure 4: N₂ adsorption–desorption isotherm with the BJH pore-size distribution of (a) SnO₂ nanoparticles and (b) bulk SnO₂.

(O_V) [35, 36]. The O_V/O_L ratio in SnO₂ nanoparticles is 48:52, which is much higher than that in bulk SnO₂ (28:72). This result further explains the formation of O_V on SnO₂

nanoparticles. The negative shifting of 0.2 eV can be seen from the binding energy of Sn 3d_{5/2} (487.36 eV) and Sn 3d_{3/2} (495.71 eV) in the SnO₂ nanoparticles in comparison to Sn

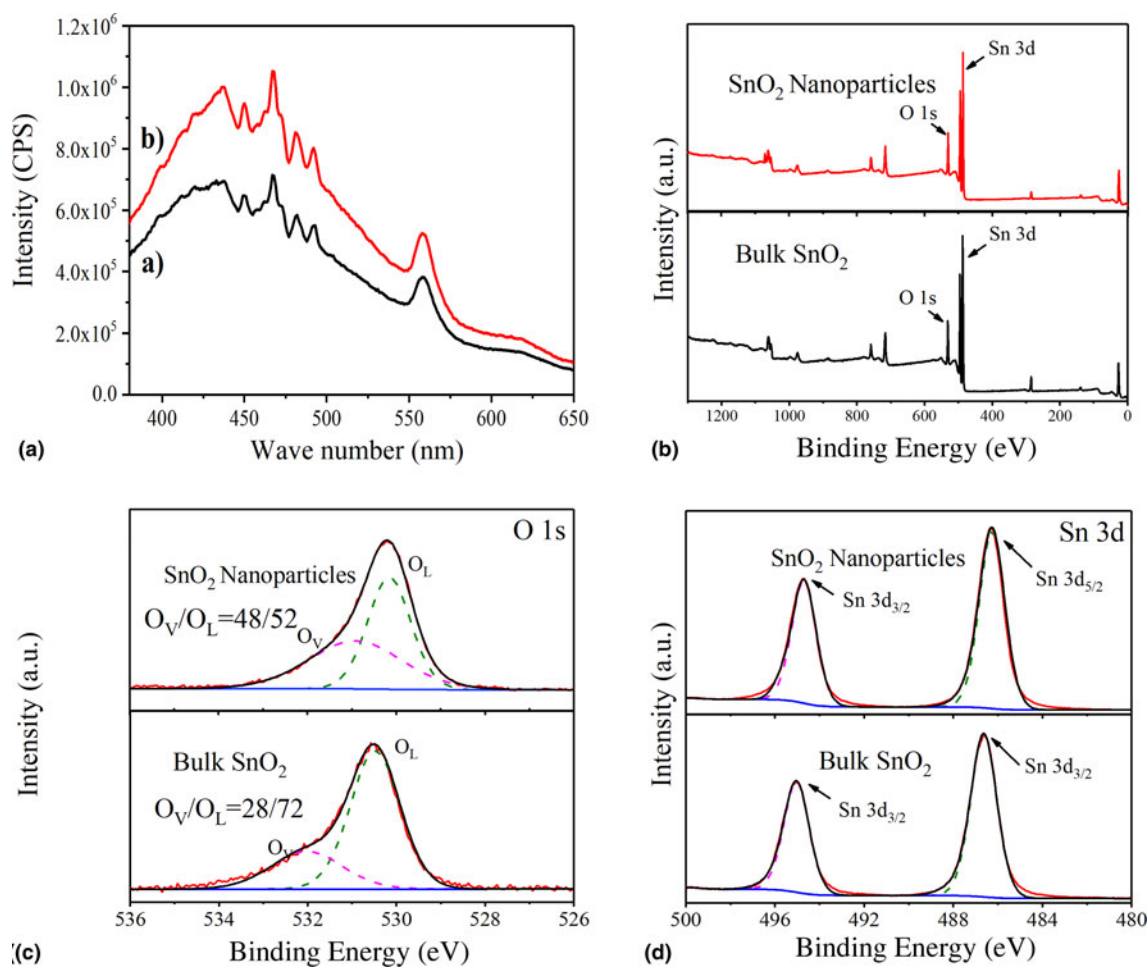


Figure 5: (a) Photoluminescence spectra of (a) SnO₂ nanoparticles and (b) bulk SnO₂ at room temperature, $\lambda_{ex} = 325$ nm; (b) the survey spectra of the samples; (c) the XPS spectra of O 1s for SnO₂ nanoparticles and bulk SnO₂; and (d) the Sn core level (3d) of the samples.

$3d_{5/2}$ (487.16 eV) and Sn $3d_{3/2}$ (495.51 eV) in the bulk SnO₂ [Fig. 5(d)] [27]. Defects at metal oxide surfaces are believed to significantly influence the surface properties, such as heterogeneous catalysis, corrosion inhibition, and gas sensing [37]. The existence of oxygen vacancies may result in the adsorptions of oxygen, and then enhance the gas response of the sensor.

Gas sensitivity

The operating temperature has a great impact on the response behavior of gas sensors by changing the reaction kinetics of gas molecule and oxygen adsorbed on the material surface [38]. To find the best temperature of the material, the sensitivity of SnO₂ nanoparticles and bulk SnO₂ to 50 ppm formaldehyde at different temperatures were tested. Figure 6(a) shows that the response of the two sensors increases at first and then decreases with the change of working temperature in the temperature range from 130 to 330 °C. For SnO₂ nanoparticles, when the temperature is lower than 180 °C, the oxygen adsorption rate is greater than the desorption rate. With the increase of temperature, the molecular weight of oxygen adsorbed on the surface of the gas-sensing material increases, and the sensitivity of gas-sensing materials increases. When the temperature reaches 180 °C, the adsorption–desorption rate reaches equilibrium and the sensitivity reaches the maximum. When the temperature is higher than 180 °C, the oxygen adsorption rate is weaker than the desorption rate, and the adsorbed oxygen molecules are desorbed, so the sensitivity decreases with the increase of temperature. Similarly, for bulk SnO₂ nanorods, 230 °C is the best working temperature. It is found that the SnO₂ nanoparticles sensor has a high response to the HCHO of 50 ppm in the operating temperature range of 40 and 250 °C, and the maximum response is 79 at 180 °C. At the same operating temperature, the response value of the SnO₂ nanoparticles sensor is about nine times that of the bulk SnO₂. Even at the optimum operating temperature of 230 °C for the bulk SnO₂ sensor, the nanoparticles sensor still has a high response to 50 ppm formaldehyde (35), which is about four times higher than that of the bulk SnO₂ sensor (9). For

nanoparticles, the best working temperature is 180 °C, but from Fig. 6(b), the response–recovery time of nanoparticles is close to 60 s at 180 °C, while the response time is 20 s and recovery time is 23 s at 230 °C [Fig. 6(c)]. Thus, the operating temperature of 230 °C was selected as the optimum operating temperature for subsequent testing.

Figures 7(a) and 7(b) show the response–recovery curve and the sensitivity curve of SnO₂ nanoparticles to different concentrations of formaldehyde at 230 °C. It can be seen from Fig. 7(a) that the response value of the sample increases rapidly with the injection of formaldehyde, and when formaldehyde is released, the voltage of the sample increases, and the response value can immediately return to the initial value. It is clearly evident that the curve exhibits a stepwise change upon exposing the sensor to different concentrations of formaldehyde. The response amplitude of the sensor increases gradually with increasing the gas concentration from 1 to 500 ppm. It can be obtained from Fig. 7(b), the sensitivity of SnO₂ nanoparticles increases with the increase of formaldehyde concentration, and the response to 1 ppm formaldehyde at 230 °C is 2.5, which can be used at low concentration. The gas response (y) as a function of HCHO concentration ranging from 1 to 500 ppm (x) was well fitted by using the equation $y = abx/(1 + bx)$, where a is the maximum adsorption amount, b is the adsorption constant, and x is the gas concentration. This can be understood as the surface coverage of adsorbed molecules followed the Langmuir isotherm model, and the specific equation is showed as followed: $y = 75.87 \times 0.0138x / (1 + 0.0138x)$, $R^2 = 0.988$

At a lower concentration, the sensor exhibits a linear relation between the sensor response and the formaldehyde concentration. At higher concentration, the surface coverage tends to saturate and, hence, leads to a saturation response.

Gas-sensing repeatability is the another important parameter to evaluate the gas-sensing ability of semiconductor materials. Therefore, the repeatability of the SnO₂ nanoparticles gas sensor was studied, and 50 ppm HCHO was tested for five times under the same conditions. In Fig. 7(c), the response time and the recovery time as well as the response values are

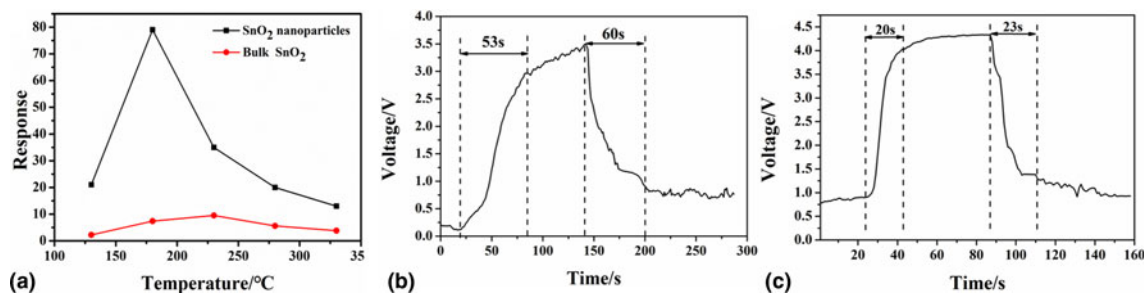


Figure 6: (a) Sensitivity of SnO₂ nanoparticles and bulk SnO₂ to 50 ppm formaldehyde under different test temperatures and (b) and (c) response–recovery curves of the SnO₂ nanoparticles sensor to 50 ppm formaldehyde at (a) 180 °C and (b) 230 °C.

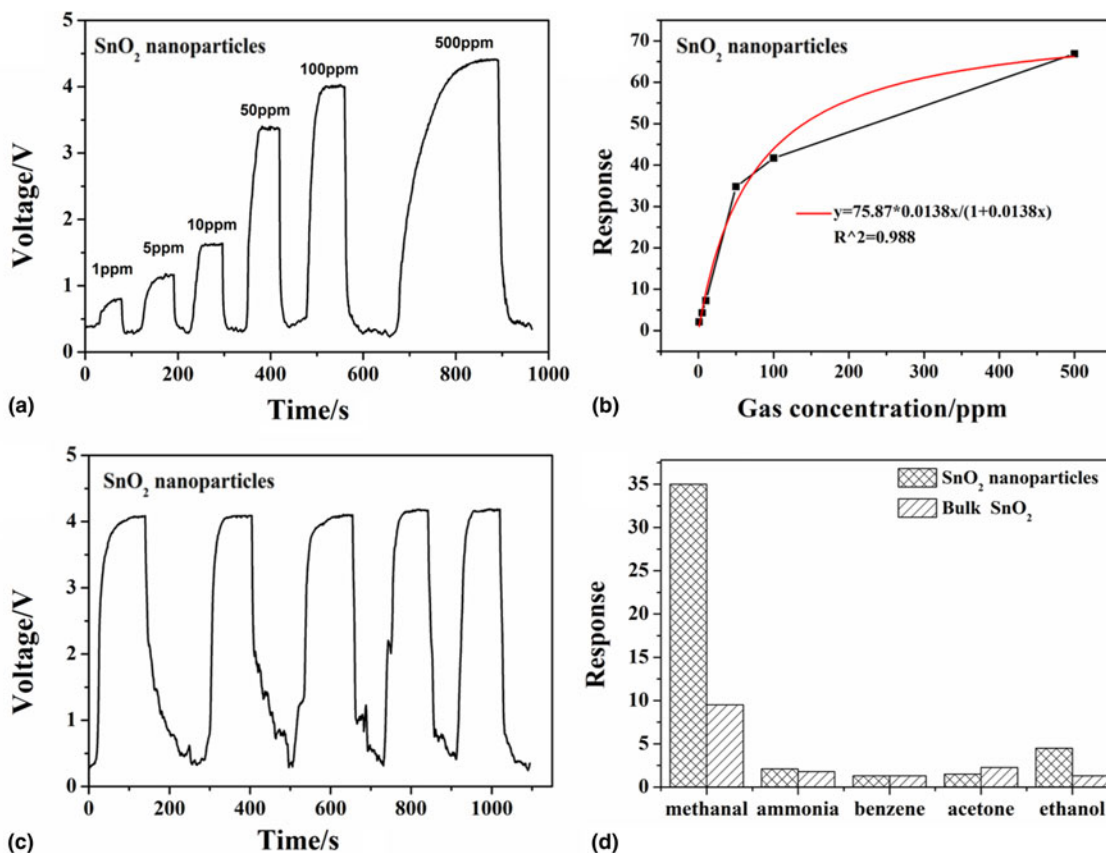


Figure 7: Gas sensitive performance of the SnO₂ nanoparticles sensor and the bulk SnO₂ sensor at 230 °C: (a) the response–recovery curve of SnO₂ nanoparticles, (b) the sensitivity curve of the SnO₂ nanoparticles sensor to different concentrations of formaldehyde, (c) repeatability of the SnO₂ nanoparticles sensor to 50 ppm formaldehyde, and (d) response values of the SnO₂ nanoparticles and bulk SnO₂ sensors to different gases (both gas concentrations are 50 ppm).

almost reproducible. The results show that the sensor has good reversibility and repeatability for the detection of formaldehyde. The response of the sensor fully recovered to the pristine level, after being exposed in HCHO and air atmosphere for several cycles.

Gas selectivity is an important index to evaluate gas sensitivity. To detect the selectivity of samples, the sensitivities of SnO₂ nanoparticles and bulk SnO₂ to different 50 ppm gases were tested at 230 °C. It can be seen from Fig. 7(d) that SnO₂ nanoparticles and bulk SnO₂ nanorods have responses to formaldehyde, ammonia, benzene, acetone, and ethanol, and the response to formaldehyde is significantly higher than that of other gases. The sensitivity (35) of the SnO₂ nanoparticles sensor to formaldehyde is about six times that of ethanol (5.6), 15 times that of the other three gases, indicating that the prepared SnO₂ nanoparticles sensor has better selectivity. The existence of oxygen defects in materials may increase the total ionic potential of the material, resulting in a close connection between the material and the adsorbed oxygen molecules (such as O₂, O₂⁻, O⁻, and O²⁻). Therefore, in equilibrium, stronger Bronsted acid is needed to take away more adsorbed oxygen. The acidity of formaldehyde is stronger than that of

ethanol and acetone (the pK_a values of formaldehyde, ethanol, and acetone are 13.27, 15.5, and 19.3, respectively) [39, 40]. Sensitive material is exposed to the target gas, formaldehyde molecules can consume more adsorbed oxygen, resulting in a higher response at relatively low temperatures. In the presence of oxygen defects in materials, the corresponding defect site/state becomes the most favorable defect site/state for the adsorption of the target gas. In addition, each oxygen vacancy provides two electrons, giving more electrons to SnO₂ nanoparticles, which is beneficial to the formation of adsorbed oxygen. Once the sensor is exposed to reducing gas molecules, the latter is oxidized by ionized oxygen species adsorbed on the surface, resulting in higher resistance.

Stability is also an important factor for the gas sensor. Good stability needs the reliability guarantee of the material. Figure 8(a) shows gas-sensing stability of the SnO₂ nanoparticles sensor to 50 ppm formaldehyde. It can be seen that the responses of the sensor had an acceptable change after a pulse test for 42 days. Due to COVID-19, the test was interrupted for a certain period of time. After a short pause, the sensitivity of the sensor decreased, but in the subsequent tests, we found that the decrease in sensitivity is lower, indicating good

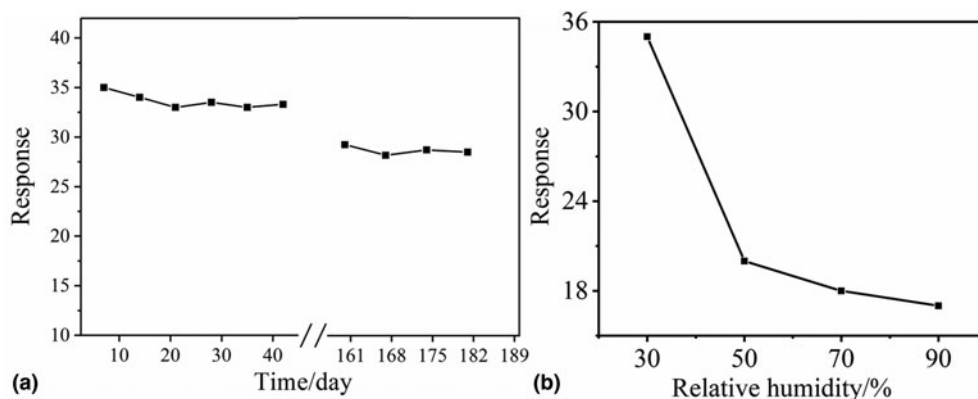


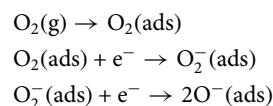
Figure 8: (a) Long-term stability of the SnO₂ nanoparticles sensor to 50 ppm formaldehyde and (b) sensor response of SnO₂ nanoparticles upon exposure to 50 ppm of formaldehyde under different RHs at 230 °C.

stability of the sensor. Humidity is generally a significant influence on MOS chemiresistive sensors as the surface of metal oxides is reactive to water. The fluctuating level of humidity brings a challenge to the operation of MOS sensors in real-world environments. To investigate the humidity effect of the sensor materials developed in this study, SnO₂ nanoparticles was tested toward 50 ppm of formaldehyde under a wide range of humidity, 30%–90% RH, as shown in Fig. 8(b). Different RH exhibits a large influence on the sensing performance, the sensor response manifests a decrease with the increase of RH, which is due to the competitive adsorption of water molecules on the surface of sensor materials. However, the response still keeps at about 17 even under the high humidity environment of 90%.

The comparison of the sensing performances of various SnO₂-based gas sensors toward formaldehyde and other systems are performed in Table 1. It was worth noting that the sensor fabricated in this work exhibited better sensing performance compared to that were reported in the references. Obviously, the response of the SnO₂ nanoparticles was much higher than those of porous SnO₂ nanospheres [41], porous flower-like SnO₂ [42], Tin oxide nanofibers [43], SnO₂ nanowires [43], hollow SnO₂ nanofibers [44], SnO₂ microspheres [15], and SnO₂ nanosheets [45]. The gas-sensing response

enhancement may be attributed to a large specific surface area and more active centers obtained from the enhanced oxygen vacancy defects on the porous nanostructure as shown in PL spectra.

The gas-sensing mechanism can be attributed to the resistance change of gas-sensing materials caused by the adsorption and desorption of gas molecules on the semiconductor surface. When SnO₂ nanoparticles are exposed to air, oxygen molecules can capture electrons in the conduction band and form an electron depletion layer induced by chemisorbed oxygen (O₂⁻, O⁻ and O²⁻) on the surface, as illustrated in Fig. 9(a). The SnO₂ nanoparticles sensor shows a very high resistance state (R_a) in ambient air because the surface layer along the diameter direction is completely depleted, which leads to the decrease of charge carrier concentration. This process, shown in Fig. 9(a), can be represented as follows:



Once exposed to the reducing gas (HCHO in this paper), the pre-adsorbed oxygen on the surface of SnO₂ will react with HCHO to form CO₂ and H₂O, which induces HCHO to directly inject electrons into the conduction band of SnO₂

Table 1: Comparison of the sensing performances of various SnO₂-based gas sensors toward formaldehyde.

Materials	Operating temperature (°C)	Concentration (ppm)	Resistance (R _a /R _g)	Response/Recovery (s)	Test system	Reference
Porous SnO ₂ nanospheres	260	10	7.6	13/14	Built by themselves	[41]
Porous flower-like SnO ₂	240	100	24.8	9/13	ART-2000A	[42]
Tin oxide nanofibers	200	50	19.6	100/90	Built by themselves	[43]
SnO ₂ nanowires	270	10	2.45	210/390	Labview© via GPIB	[43]
Hollow SnO ₂ nanofibers	180	100	5.4	12/22	CGS-8	[44]
SnO ₂ microspheres	160	100	3.6	20/45	CGS-8	[15]
SnO ₂ microspheres	200	100	38.3	17/25	WS-30A	[31]
SnO ₂ nanosheets	200	50	38	40/145	WS-30A	[45]
SnO ₂ nanoparticles	230	50	35	20/23	WS-30A	This work
SnO ₂ nanoparticles	180	50	79	53/60	WS-30A	This work

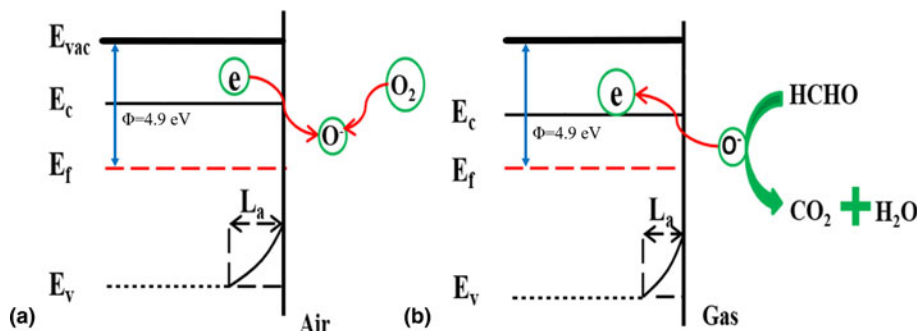
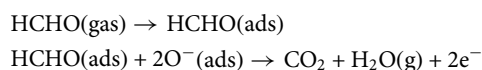


Figure 9: Schematic diagram of the proposed gas-sensing mechanism of the SnO₂ nanoparticles-based sensor: (a) in air and (b) in HCHO.

nanoparticles. Therefore, this process leads to a shrinking electron transport barrier and a reduced electron depletion barrier, which greatly reduces the thickness of the depletion layer, resulting in a low resistance state (R_g). As shown in Fig. 9(b), the surface adsorption and redaction can be described as follows:



In addition to the grain size effect, the excellent HCHO sensing properties of SnO₂ nanoparticles, especially the high responsiveness and fast reaction rate, can be attributed to the large specific surface area (42.5 m²/g), which means that more HCHO and oxygen molecules can be adsorbed on the SnO₂ surface.

Conclusion

In summary, the SnO₂ nanoparticles are successfully synthesized by a facile hydrothermal method. The size of SnO₂ nanoparticles is not more than 20 nm, and the corresponding specific surface area is 42.5 m²/g. Compared with the bulk SnO₂ sensor, the SnO₂ nanoparticles sensor exhibits significantly enhanced response toward HCHO. The response (35) of the SnO₂ nanoparticles sensor to 50 ppm HCHO is about 400% higher than that of the SnO₂ nanorods sensor (9). SnO₂ nanoparticles also have a good response to formaldehyde of low concentration, when the concentration is 1 ppm, the sensitivity can reach 2.5. The gas sensor based on SnO₂ nanoparticles is fabricated and exhibited high response, good response–recovery properties, linear dependence, repeatability, and selectivity toward HCHO at the operating temperature of 230 °C.

Experimental Sections

All the reagents (analytical-grade purity) were purchased from Shanghai Chemical Reagent Co. Ltd. (Shanghai, China) and were used without further purification. Deionizer water was used throughout the experiments.

Material synthesis

SnO₂ nanoparticles

In a typical synthesis, 1.1285 g of SnCl₂·2H₂O (5 mmol) and 2.941 g of trisodium citrate dihydrate (10 mmol) were dissolved in the mixture of 15 mL of deionized water and 15 mL of ethylene glycol. Firstly, a clear solution was obtained after magnetic stirring for 30 min. Then, the solution was transferred into a Teflon-lined stainless-steel autoclave with a capacity of 40 mL and maintained at 180 °C for 18 h. After cooling down to room temperature, the precipitate was collected, centrifuged, and washed several times with deionized water and absolute ethanol alternately, followed by drying at 80 °C for 12 h to obtain the precursor. Finally, SnO₂ nanoparticles were obtained by calcination of the precursor at 500 °C for 2 h in air.

Bulk SnO₂ contrast

A similar preparation procedure with nanoparticle except that trisodium citrate dihydrate was replaced by 0.16 g NaOH (4 mmol).

Materials characterization

Powder XRD measurements were performed with a Bruker D8 ADVANCE X-ray diffractometer (Bruker AXS GmbH, Karlsruhe, Germany) in a scanning range of 10–70° (2θ) at a rate of 0.03° (2θ)/s with Cu K_α radiation. SEM (Hitachi SU5000, Hitachi Limited, Tokyo, Japan), TEM and HRTEM (FEI Tecnai G2 f20 s-twin, 200 KV, FEI Company, Portland, Oregon, USA) were utilized for the investigation of the morphology and structure of the prepared material. At room temperature, PL measurements were performed on a Steady-State and Transient State Fluorescence Spectrometer (HORIBA TCSPC FluoroLog-3, HORIBA Jobin Yvon inc., Edison, New Jersey, USA). X-ray photoelectron spectroscopy (XPS) was conducted with Thermo Scientific ESCALAB 250Xi using Al K_α X-ray monochromator (Waltham, Massachusetts, USA). Nitrogen (N₂) adsorption–desorption study was conducted through Gemini V2380 (Micromeritics, Atlanta, Georgia, USA). The BET was used to determine the specific surface area and the pore volume.

Gas response test

Figure 1(a) shows a schematic diagram of the sensor structure. As can be seen, a pair of Au electrodes is preprinted on both sides of the alumina ceramic tube. The Ni–Cr wire heater in the ceramic tube is used to control the working temperature of the sensor. The side-heating gas sensor was made as follows: first of all, the sample and adhesive were fully ground in an agate mortar to form a gas-sensing paste. The paste was coated on the alumina ceramic tube and 15 min was dried under IR radiation afterward. Next, the alumina ceramic tube was sintered at 500 °C for 2 h, and then welded to the pedestal. Finally, the sensors were aged at 300 °C for 7 days to increase its stability.

Gas-sensing properties were measured by a WS-30A system (Weisheng Instruments Co., Zhengzhou, China) under laboratory condition. The relative humidity of the test is about 30–40%. The circuit voltage (V_c) was set at 5 V, and the output voltage (V_{out}) was set as the terminal voltage of the load resistor (R_L). The test gas was injected into a test chamber using a micro syringe after the baseline of the sensor was stable. The desired concentrations of the testing gas are obtained by the volume of the analyte solution. The analyte solution was evaporated by an evaporator. At the same time, two fans were installed to make the gas homogeneous. The gas response of the sensor in this paper was defined as $S = R_a/R_g$ (reducing gases) or $S = R_g/R_a$ (oxidizing gases). The response or recovery time was expressed as the time taken for the sensor output to reach 90% of its saturation after applying or switching off the gas in a step function.

Acknowledgments

The research was supported by the National Natural Science Foundation of China (No. 51762005), the Natural Science Foundation of Guangxi Province, China (2017GXNSFAA198254), General Project of Teaching Research of Anhui Province (KJ2018B13 and KJ2017B06), and College Students Innovation and Entrepreneurship Training Project (201910377033).

References

1. N. Li, Q. Xiang, Z.X. Cheng, X.H. Wang, and J.Q. Xu: Synthesis of porous SnO₂ hollow sphere materials and gas sensing properties of formaldehyde. *J. Zhengzhou Univ.* **40**, 27–31 (2019).
2. H. Chen, L. Sun, G.D. Li, and X.X. Zou: Well-tuned surface oxygen chemistry of cation off-stoichiometric spinel oxides for highly selective and sensitive formaldehyde detection. *Chem. Mater.* **30**, 2018–2027 (2018).
3. Z. Zhang: Gas-sensing properties and in situ diffuse reflectance infrared Fourier transform spectroscopy study of formaldehyde adsorption and reactions on SnO₂ films. *J. Mater. Res.* **29**, 139–147 (2013).

4. C.P. Gu, W.M. Guan, X.S. Liu, L.L. Gao, L.Y. Wang, J.J. Shim, and J.R. Huang: Controlled synthesis of porous Ni-doped SnO₂ microstructures and their enhanced gas sensing properties. *J. Alloy Compd.* **692**, 855–864 (2017).
5. A.T. Guntner, V. Koren, K. Chikkadi, M. Righettoni, and S.E. Pratsinis: E-nose sensing of low-ppb formaldehyde in gas mixtures at high relative humidity for breath screening of lung cancer? *ACS Sens.* **1**, 528–535 (2016).
6. P.K. Kannan: An impedance sensor for the detection of formaldehyde vapor using ZnO nanoparticles. *J. Mater. Res.* **32**, 2800–2809 (2017).
7. X.G. Jiang, C.Y. Li, Y. Chi, and J.H. Yan: TG–FTIR study on urea–formaldehyde resin residue during pyrolysis and combustion. *J. Hazard. Mater.* **173**, 205–210 (2010).
8. G.R. Mohimann: Formaldehyde detection in air by laser induced fluorescence. *Appl. Spectrosc.* **39**, 98–101 (1985).
9. P.R. Chung, C.T. Tzeng, M.T. Ke, and C.Y. Lee: Formaldehyde gas sensors: A review. *Sensors* **13**, 4468–4484 (2013).
10. B. Mann and M.L. Grajeski: New chemiluminescent derivatizing agent for the analysis of aldehyde and ketones by high-performance liquid chromatography with peroxoxalate chemiluminescence. *J. Chromatogr.* **386**, 149–158 (1987).
11. E. Norkus, A. Vaskelis, and R. Pauliukaite: Polarographic determination of formaldehyde according to the anodic oxidation wave in alkaline solutions. *Electroanalysis* **1**, 1447–1449 (1999).
12. C. Liu, A.W. Cheng, X.K. Xia, Y.F. Liu, S.W. He, X. Guo, and Y.S. Ji: Development of a facile and sensitive fluorometric derivatization reagent for detecting formaldehyde. *Anal. Methods* **8**, 2764–2770 (2016).
13. L.X. Zhang, J.H. Zhao, J.F. Zheng, L. Li, and Z.P. Zhu: Shuttle-like ZnO nano/microrods: Facile synthesis, optical characterization and high formaldehyde sensing properties. *Appl. Surf. Sci.* **258**, 711–718 (2011).
14. L. Wang: Polymer g-C₃N₄ wrapping bundle-like ZnO nanorod heterostructures with enhanced gas sensing properties. *J. Mater. Res.* **4**, 23 (2018).
15. Y. Lin, W. Wei, Y.J. Li, F. Li, J.R. Zhou, D.M. Sun, Y. Chen, and S.P. Ruan: Preparation of Pd nanoparticle-decorated hollow SnO₂ nanofibers and their enhanced formaldehyde sensing properties. *J. Alloys Compd.* **651**, 690–698 (2015).
16. S.M. Wang, J. Chao, W. Cui, L.L. Fan, X.F. Li, and D.J. Li: Oxygen vacancies and grain boundaries potential barriers modulation facilitated formaldehyde gas sensing performances for In₂O₃ hierarchical architectures. *Sens. Actuat. B* **255**, 159–165 (2018).
17. S.P. Kim, M.Y. Choi, and H.C. Choi: Photocatalytic activity of SnO₂ nanoparticles in methylene blue degradation. *Mater. Res. Bull.* **74**, 85–89 (2016).
18. Q. Jiang, X.W. Zhang, and J.B. You: SnO₂: A wonderful electron transport layer for perovskite solar cells. *Small* **14**, 1801154 (2018).

19. **B.J. Li, G.Y. Yang, L.J. Huang, W. Zu, and N.F. Ren:** Performance optimization of SnO₂: F thin films under quasi-vacuum laser annealing with covering a transparent PET sheet: A study using processing map. *Appl. Surf. Sci.* **509**, 145334 (2020).
20. **P.H. Phuoc, C.M. Huang, N.V. Toan, N.V. Duy, N.D. Hoa, and N.V. Hieu:** One-step fabrication of SnO₂ porous nanofiber gas sensors for sub-ppm H₂S detection. *Sens. Actuat. A* **303**, 111722 (2020).
21. **P. Sun, Y. Cao, J. Liu, Y.F. Sun, J. Ma, and G.Y. Lu:** Dispersive SnO₂ nanosheets: Hydrothermal synthesis and gas sensing properties. *Sens. Actuat. B* **156**, 779–783 (2011).
22. **F. Gao, G.H. Qin, Y.H. Li, Q.P. Jiang, L. Luo, K. Zhao, Y.J. Liu, and H.Y. Zhao:** One-pot synthesis of La-doped SnO₂ layered nanoarrays with an enhanced gas sensing performance toward acetone. *RSC Adv.* **6**, 10298–10310 (2016).
23. **G.T. Ang, G.H. Toh, M.Z.A. Bakar, A.Z. Abdullah, and M.R. Othman:** High sensitivity and fast response SnO₂ and La-SnO₂ catalytic pellet sensors in detecting volatile organic compounds. *Process Saf. Environ. Prot.* **89**, 186–192 (2011).
24. **J.Q. Xu, D. Wang, L.P. Qin, W.J. Yu, and Q.Y. Pan:** SnO₂ nanorods and hollow spheres: Controlled synthesis and gas sensing properties. *Sens. Actuat. B* **137**, 490–495 (2009).
25. **Z.U. Abideen, J.-H. Kim, and S.S. Kim:** Optimization of metal nanoparticle amount on SnO₂ nanowires to achieve superior gas sensing properties. *Sens. Actuat. B* **238**, 374–380 (2017).
26. **Y. Zeng, Y.Z. Wang, L. Qiao, Y.F. Bing, B. Zou, and W.T. Zeng:** Synthesis and the improved sensing properties of hierarchical SnO₂ hollow nanosheets with mesoporous and multilayered interiors. *Sens. Actuat. B* **222**, 354–361 (2016).
27. **G. Li, Z. Cheng, Q. Xiang, L. Yan, X. Wang, and J. Xu:** Bimetal PdAu decorated SnO₂ nanosheets based gas sensor with temperature-dependent dual selectivity for detecting formaldehyde and acetone. *Sens. Actuat. B* **283**, 590–601 (2019).
28. **Q. Wang, N. Yao, D.M. An, Y. Li, Y.L. Zou, X.X. Lian, and X.X. Tong:** Enhanced gas sensing properties of hierarchical SnO₂ nanoflower assembled from nanorods via a one-pot template-free hydrothermal method. *Ceram. Int.* **42**, 15889–15896 (2016).
29. **J. Hu, X. Li, X. Wang, Y. Li, Q. Li, and F. Wang:** Hierarchical aloe-like SnO₂ nanoflowers and their gas sensing properties. *J. Mater. Res.* **33**, 1433–1441 (2018).
30. **C.L. Zhang, J. Wang, R.J. Hu, Q. Qiao, and X.G. Li:** Synthesis and gas sensing properties of porous hierarchical SnO₂ by grapefruit exocarp biotemplate. *Sens. Actuat. B* **222**, 1134–1143 (2016).
31. **Y.X. Li, N. Chen, D.Y. Deng, X.X. Xing, X.C. Xiao, and Y.D. Wang:** Formaldehyde detection: SnO₂ microspheres for formaldehyde gas sensor with high sensitivity, fast response/recovery and good selectivity. *Sens. Actuat. B* **238**, 264–273 (2017).
32. **H. Li, D. Zhu, and Z. Yang:** Synthesis and properties of SnO₂ aerogels via ambient pressure drying of sol–gel. *J. Mater. Res.* **33**, 4192–4198 (2018).
33. **Y. Cui, M. Zhang, X. Li, B. Wang, and R. Wang:** Investigation on synthesis and excellent gas-sensing properties of hierarchical Au-loaded SnO₂ nanoflowers. *J. Mater. Res.* **34**, 2944–2954 (2019).
34. **S.H. Luo, J.Y. Fan, W.L. Liu, M. Zhang, Z.T. Song, C.L. Liu, X.L. Wu, and P. Chu:** Synthesis and low-temperature photoluminescence properties of SnO₂ nanowires and nanobelts. *Nanotechnology* **17**, 1695–1699 (2006).
35. **M. Xiao, L. Zhang, B. Luo, M. Lyu, Z. Wang, H. Huang, S. Wang, A. Du, and L. Wang:** Molten-salt-mediated synthesis of an atomic nickel Co-catalyst on TiO₂ for improved photocatalytic H₂ evolution. *Angew. Chem. Int. Ed.* **59**, 7230–7236 (2020).
36. **Y. Fang, Z. Liu, J. Han, Z. Jin, Y. Han, F. Wang, Y. Niu, Y. Wu, and Y. Xu:** High-performance electrocatalytic conversion of N₂ to NH₃ using oxygen-vacancy-rich TiO₂ in situ grown on Ti₃C₂Tx MXene. *Adv. Energy Mater.* **9**, 1–9 (2019).
37. **F. Gong, M. Liu, L. Gong, D. Li, Y. Li, and F. Li:** SnO₂ nanomulberries anchored onto RGO nanosheets for lithium ion batteries. *J. Mater. Res.* **35**, 20–30 (2019).
38. **Y. Zhang, J.Q. Xu, Q. Xiang, H. Li, Q.Y. Pan, and P.C. Xu:** Brush-Like hierarchical ZnO nanostructures: synthesis, photoluminescence and gas sensor properties. *J. Phys. Chem. C* **113**, 430–435 (2009).
39. **H. Li, W.Y. Xie, B. Liu, Y.R. Wang, S.H. Xiao, X.C. Duan, Q.H. Li, and T.H. Wang:** Ultra-fast and highly-sensitive gas sensing arising from thin SnO₂ inner wall supported hierarchical bilayer oxide hollow spheres. *Sens. Actuat. B* **240**, 349–357 (2017).
40. **H. Chen, J. Hu, G.D. Li, Q. Gao, C. Wei, and X. Zou:** Porous Ga-In bimetallic oxide nanofibers with controllable structures for ultrasensitive and selective detection of formaldehyde. *ACS Appl. Mater. Interfaces* **9**, 4692–4700 (2017).
41. **Z.P. Li, Q.Q. Zhao, W.L. Fan, and J.H. Zhan:** Porous SnO₂ nanospheres as sensitive gas sensors for volatile organic compounds detection. *Nanoscale* **3**, 646–1652 (2011).
42. **H.B. Ren, W. Zhao, L.Y. Wang, S.O. Ryu, and C.P. Gu:** Preparation of porous flower-like SnO₂ micro/nano structures and their enhanced gas sensing property. *J. Alloys Compd.* **653**, 611–618 (2015).
43. **H.Y. Du, J. Wang, P. Yu, N.S. Yu, Y.H. Sun, and J.L. Tian:** Investigation of gas sensing materials tin oxide nanofibers treated by oxygen plasma. *J. Nanopart. Res.* **16**, 2216 (2014).
44. **I. Castro-Hurtado, J. Herrán, G.G. Mandayo, and E. Castáno:** SnO₂-nanowires grown by catalytic oxidation of tin sputtered thin films for formaldehyde detection. *Thin Solid Films* **520**, 792–4796 (2012).
45. **R. Xu, L.X. Zhang, M.W. Li, Y.Y. Yin, J. Yin, M.Y. Zhu, J.J. Chen, Y. Wang, and L.J. Bie:** Ultrathin SnO₂ nanosheets with dominant high-energy {001} facets for low temperature formaldehyde gas sensor. *Sens. Actuat. B* **289**, 186–194 (2019).